Chemical Science

ROYAL SOCIETY OF CHEMISTRY

EDGE ARTICLE

View Article Online
View Journal | View Issue

Cite this: *Chem. Sci.*, 2024, **15**, 9830

All publication charges for this article have been paid for by the Royal Society of Chemistry

Received 6th March 2024
Accepted 30th April 2024

DOI: 10.1039/d4sc01560f

rsc.li/chemical-science

Facet-dependent synthesis of H_2O_2 from H_2 and O_2 over single Pt atom-modified Pd nanocrystal catalysts†

Ying Zhang,[a] Qingdi Sun,[a] Ziyue Wang,[a] Guanghui Guo,[a] Hao Liu,[a] Xiaohui He *[ac] and Hongbing Ji *[ab]

Hydrogen peroxide (H_2O_2) is one of the most valuable clean energy sources with a rapidly growing requirement in industry and daily life. The direct synthesis of H_2O_2 from hydrogen and oxygen is considered to be an economical and environmentally friendly manufacturing route to replace the traditional anthraquinone method, although it remains a formidable challenge owing to low H_2O_2 selectivity and production. Here, we report a catalyst consisting of Pd(111) nanocrystals on TiO_2 modified with single Pt atoms ($Pt_1Pd(111)/TiO_2$), which displays outstanding reactivity, producing 1921.3 μmol of H_2O_2, a H_2 conversion of 62.2% and H_2O_2 selectivity of 80.3% over 30 min. Kinetic and isotope experiments confirm that the extraordinary catalytic properties are due to stronger H_2 activation (the rate-determining step). DFT calculations confirm that $Pt_1Pd(111)$ exhibits lower energy barriers for H_2 dissociation and two-step O_2 hydrogenation, but higher energy barriers for side reactions than $Pt_1Pd(100)$, demonstrating clear facet dependence and resulting in greater selectivity and amount of H_2O_2 produced.

Introduction

Hydrogen peroxide (H_2O_2) is considered to be one of the most crucial chemicals in the world. It has been widely used in various fields, including the synthesis of chemicals and pharmaceuticals, environmental protection, sterilization, and bleaching, because of its strong oxidation capability of which the exclusive byproduct is water.[1–4] The environmental friendliness and effectiveness of H_2O_2 have caused a continuous increase in its use and production.[5] Currently, more than 95% of industrial H_2O_2 production is highly dependent on the anthraquinone process, which is a large-scale multi-step process involving intense energy input, hazardous organic compounds, and highly concentrated H_2O_2 solutions.[6–10] However, it is important to note that more than two-thirds of end-use application demand is for low concentration H_2O_2 (less than 9 wt%).[11–13] Under such circumstances, environmental and economic factors have led to a strong interest in low-scale and low-energy processes to synthesize hydrogen peroxide.[14,15]

Compared with conventional processes, the direct synthesis of H_2O_2 (DSHP) is considered to be a green and appealing alternative clean manufacturing route that can potentially produce H_2O_2 in a ready-to-use, eco-friendly manner.[16–18] Despite the above-mentioned advantages, the low yield of H_2O_2 owing to its thermodynamically favorable side reactions (including the dissociation of O_2 to form H_2O, H_2O_2 hydrogenation, and H_2O_2 decomposition, as shown in Scheme 1) means that the DSHP remains a tremendous challenge.[19] Pd is regarded as a credible catalytic component for the DSHP owing to its superior hydrogen activation ability, especially at low operating temperatures. However, pure Pd is not only active in the synthesis of H_2O_2 but also in the aforementioned side reactions. Therefore, researchers improved the DSHP catalytic performance by incorporating a second component and found that

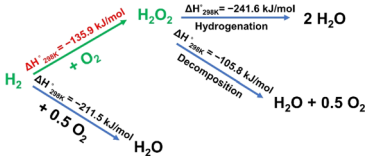

Scheme 1 Reactions and corresponding enthalpies in the direct synthesis of H_2O_2.

[a]Key Laboratory of Bioinorganic and Synthetic Chemistry of Ministry of Education, Fine Chemical Industry Research Institute, School of Chemistry, IGCME, Sun Yat-sen University, Guangzhou 510275, China. E-mail: jihb@mail.sysu.edu.cn; hexiaohui@mail.sysu.edu.cn

[b]State Key Laboratory Breeding Base of Green-Chemical Synthesis Technology, Institute of Green Petroleum Processing and Light Hydrocarbon Conversion, College of Chemical Engineering, Zhejiang University of Technology, Hangzhou, 310014, P. R. China

[c]Guangdong Technology Research Center for Synthesis and Separation of Thermosensitive Chemicals, China

† Electronic supplementary information (ESI) available. See DOI: https://doi.org/10.1039/d4sc01560f

the reaction path could be regulated by finely tuning the electronic environment around the Pd species.[13,17,18,20–23] For example, Hutchings and co-workers reported a $PdSn/TiO_2$ catalyst with a layer of tin oxide wrapped around the surface of small Pd-rich particles synthesized *via* an appropriate heat treatment cycle, which could shut down the successive hydrogenation and decomposition reactions, thus improving the catalytic performance of Pd in the DSHP.[17] Lewis and co-workers reported that the introduction of base metals into a AuPd catalyst improved the catalytic performance towards the DSHP, attributing the improvement to the modification of the electronic environment of Pd.[24] Additionally, single-atom species, due to their unique electronic structures, can also be used as electronic promoters to modify the electronic structure of the active sites.[25,26] For example, Wang and co-workers reported that single Pt atoms can operate as electronic promoters to effectively modify the electronic structure of catalysts, thus improving the catalytic performance in the water-gas shift reaction.[27] However, the lack of a complete understanding of the inherent mechanism of the Pd-catalyzed DSHP has seriously hindered its practical application.[28] Therefore, more investigations are desired to further understand the structure–activity relationships in order to obtain more active, selective and stable catalysts for the DSHP.

It is also noteworthy that the surface morphology of the active sites plays an essential role in regulating the catalytic activity, as the properties of the active sites and the energetics of the reaction are ultimately determined by the exposed facets.[29–31] Nanocrystals with facet-controlled shapes can provide an accessible platform to reveal the underlying mechanisms of catalytic reactions, since the atomic arrangements and well-documented electronic configurations of specific facets are beneficial for revealing structure–activity relationships.[32–36]

Inspired by the above discussion, we aim to develop a DSHP catalyst with high performance while providing an in-depth understanding of the reaction mechanism. Herein, we employ single Pt atoms as promoters to modify the surface interface structure of Pd nanocrystals with different exposed facets for the DSHP. Interestingly, Pt_1Pd nanocrystal catalysts with Pd(111) surfaces ($Pt_1Pd(111)/TiO_2$) not only showed a prominent facet-dependent effect but also exhibited outstanding catalytic activity when compared to catalysts with Pd(100) surfaces ($Pt_1Pd(100)/TiO_2$). The amount of generated H_2O_2 reached 1921.3 μmol for 30 min. Kinetic experiments and theoretical calculations revealed the possible mechanism by which the catalysts with $Pt_1Pd(111)$ surfaces can effectively reduce the H_2 dissociation and O_2 reduction energy barriers, thus facilitating the H_2O_2 synthesis process.

Results and discussion

Synthesis of catalysts and catalytic performance

Single Pt atom were introduced as promoters into Pd nanocrystals using a simple solvothermal method, as shown in Fig. S1,† according to a slightly modified previous report.[37] The detailed procedure is given in the catalyst preparation section in the Materials and methods. The synthesis of the $Pt_1Pd(111)$ nanocrystals was conducted in an aqueous solution containing K_2PdCl_4, $H_2PtCl_6 \cdot 6H_2O$, PVP, citric acid, and L-ascorbic acid at 120 °C for 3 h. The purified $Pt_1Pd(111)$ nanocrystals were collected as a colloidal dispersion in water. The transmission electron microscopy (TEM) images displayed mainly monodisperse octahedron-shaped nanocrystals with a size of 8.9 ± 1.0 nm (Fig. 1a–c). High-resolution TEM images (Fig. 1d–f) revealed the individual crystalline character of the nanocrystals and that they have a lattice spacing of 2.25 Å, which was in good agreement with the Pd metal phase (2.26 Å of PDF#87-0643 for Pd(111)). The successful preparation of the $Pt_1Pd(111)$ nanocrystals also was certified by the X-ray diffraction (XRD) results (Fig. S2a†). Next, $Pt_1Pd(111)/TiO_2$ was obtained by impregnating the $Pt_1Pd(111)$ nanocrystals onto TiO_2. The inductively coupled plasma optical emission spectrometry (ICP-OES) results indicated that the Pd loading was 3.3 wt% and the Pt loading was 0.09 wt% (Table S1†), which were close to the nominal loadings. The dark- and bright-field scanning transmission electron microscopy (STEM) images and the XRD results (Fig. 1g and S2†) suggested that the $Pt_1Pd(111)$ nanocrystals were uniformly dispersed on the TiO_2 and still retained their octahedral shape. A detailed characterization of the dispersion of Pt and Pd atoms in $Pt_1Pd(111)/TiO_2$ was obtained *via* aberration-corrected high-angle annular dark-field STEM (AC HAADF-STEM). Fig. 1h showed that the individual $Pt_1Pd(111)$ nanocrystals were supported on TiO_2. Single Pt atoms on the Pd(111) surface were clearly observed and are highlighted by yellow circles in Fig. 1h. Furthermore, the elemental analysis mapping (Fig. 1i) and elemental line–scan profiles (Fig. S3†) confirmed a few Pt atoms were uniformly distributed on the surface of Pd(111).

In order to investigate the influence of the exposed facets on the DSHP, unsupported $Pt_1Pd(100)$ nanocrystals and $Pt_1Pd(100)/TiO_2$ (Pd loading of 3.4 wt% and Pt loading of 0.08 wt%, Table S1†) were synthesized *via* a similar method using KBr as a capping agent at 80 °C, as shown in Fig. S1.† The detailed structural characterization is shown in Fig. S4–6.† The TEM images showed that the cubic shaped $Pt_1Pd(100)$ nanocrystals with a size of 10.5 ± 1.8 nm and lattice spacing of 1.95 Å (1.95 Å of PDF#87-0643 for Pd(200)) were successfully prepared. STEM images and XRD indicated that the $Pt_1Pd(100)$ nanocrystals were uniformly dispersed on the TiO_2 and still retained their cubic shape. AC HAADF-STEM and elemental analysis mapping confirmed the uniform distribution of the individual Pt atoms on the Pd(100) surface. For comparison, $Pd(111)/TiO_2$ (Pd loading of 3.2 wt% and particle size of 7.8 ± 1.1 nm) and $Pd(100)/TiO_2$ (Pd loading of 3.6 wt% and particle size of 10.8 ± 1.8 nm) were also successfully synthesized by the same method without adding $H_2PtCl_6 \cdot 6H_2O$, as evidenced by TEM, STEM images and XRD (Table S1 and Fig. S7–10†).

In a typical reaction, the catalytic test of the DSHP was conducted in a 100 mL stainless-steel autoclave at 0 °C employing methanol as the solvent. Initially, $Pd(100)/TiO_2$ showed low H_2 conversion (16.8%), H_2O_2 selectivity (49.3%), productivity (2.0 mol g_{Pd}^{-1} h^{-1}), and amount of generated H_2O_2 (360.0 μmol) (Table 1, entry 1). After adding the single Pt atoms to the Pd(100) surface, the catalyst ($Pt_1Pd(100)/TiO_2$) showed

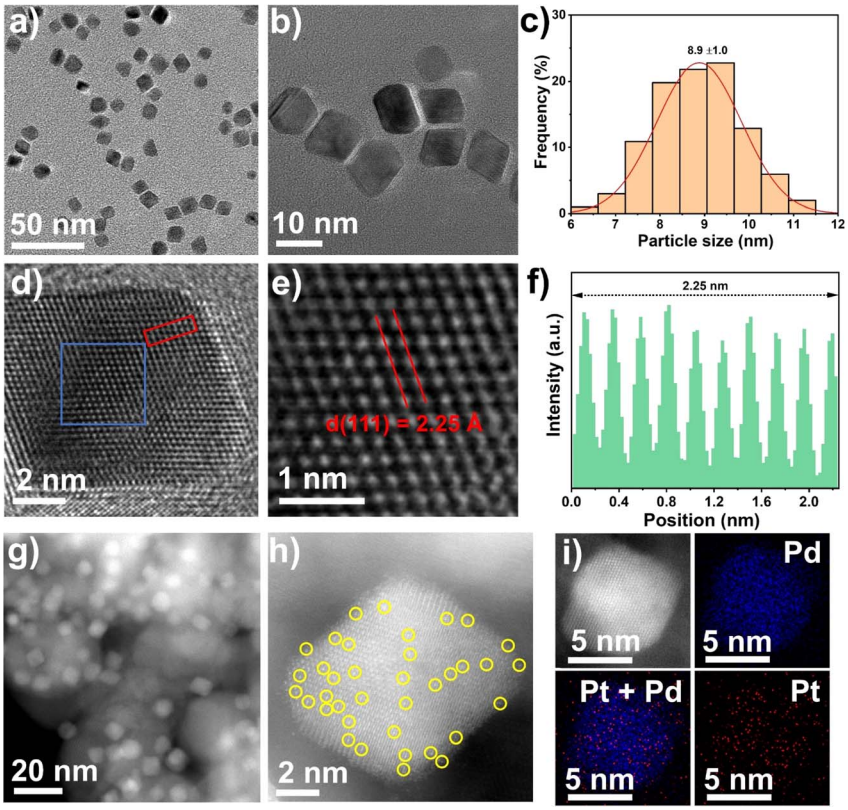

Fig. 1 Morphology and structure of the monodispersed $Pt_1Pd(111)$ nanocrystals. (a) Representative TEM image. (b and d) High-resolution TEM images. (c) $Pt_1Pd(111)$ nanocrystals particle size distribution. (e) Magnified TEM image of the blue box from (d). (f) Intensity profile of the red box from (d). (g) The dark-field STEM image of the $Pt_1Pd(111)$ nanocrystals supported on TiO_2 ($Pt_1Pd(111)/TiO_2$). (h) AC HAADF-STEM images of $Pt_1Pd(111)/TiO_2$, single Pt atoms are highlighted by the yellow circles. (i) EDS mapping of $Pt_1Pd(111)/TiO_2$.

higher activity (H_2 conversion of 38.2%, H_2O_2 selectivity of 60.0%, productivity of 5.8 mol g_{Pd}^{-1} h^{-1}, and generated H_2O_2 of 985.0 μmol) (Table 1, entry 3) than $Pd(100)/TiO_2$. Interestingly, the catalytic performance (H_2 conversion of 24.4%, H_2O_2 selectivity of 49.5%, productivity of 3.3 mol g_{Pd}^{-1} h^{-1}, generated H_2O_2 of 525.0 μmol on $Pd(111)/TiO_2$, and H_2 conversion of 62.2%, H_2O_2 selectivity of 80.3%, productivity of 11.8 mol g_{Pd}^{-1} h^{-1}, generated H_2O_2 of 1921.3 μmol on $Pt_1Pd(111)/TiO_2$) (Table 1, entries 2 and 4) were obviously enhanced by adjusting the exposed Pd(100) surface to Pd(111) surface, implying a facet-dependent synthesis of H_2O_2 from H_2 and O_2. Moreover, the above results also implied that the presence of the Pt single atoms improved the selectivity and activity of the H_2O_2 synthesis. To the best of our knowledge, the amount of

Table 1 Direct H_2O_2 synthesis performance using $Pd(100)/TiO_2$, $Pd(111)/TiO_2$, $Pt_1Pd(100)/TiO_2$, $Pt_1Pd(111)/TiO_2$, and reported catalysts

Entry	Catalyst	H_2 conversion (%)	H_2O_2 selectivity (%)	Productivity (mol g_{Pd}^{-1} h^{-1})	Amount of H_2O_2 (μmol)	Time (min)	Reference
1	$Pd(100)/TiO_2$	16.8	49.3	2.0	360.0	30	This work[a]
2	$Pd(111)/TiO_2$	24.4	49.5	3.3	525.0	30	This work[a]
3	$Pt_1Pd(100)/TiO_2$	38.2	60.0	5.8	985.0	30	This work[a]
4	$Pt_1Pd(111)/TiO_2$	62.2	80.3	11.8	1921.3	30	This work[a]
5	Pd_6Pb NRs/TiO_2-H-A	40.0	56.7	5.7	447.7	30	1
6	0.1%O–Pd/TiO_2	3.9	>99	115	143.8	30	7
7	PdL/PdSn-NW	22.1	95.3	12.8	656.0	15	14
8	3 wt% Pd-2 wt% Sn/TiO_2	9.0	96.0	2.0	300.0	30	17
9	AuPd@HZSM-5	28.0	90.0	1.1	396.0	30	21
10	Pd-HHDMA/C	9.7	79.8	12.8	108.8	30	38
11	$Pd-Sb/TiO_2$	13.9	73.0	1.6	388.0	10	39

[a] The reaction conditions of H_2O_2 synthesis: 10 mL CH_3OH, 0.02 M HCl, 2.9 MPa 5% H_2/N_2, 1.1 MPa 25% O_2/N_2, $T = 0$ °C, catalyst weight: 10 mg, stirring: 1200 rpm, reaction time: 30 min.

generated H_2O_2 on $Pt_1Pd(111)/TiO_2$ was notable compared to previous reports[1,7,14,17,21,38,39] under similar reaction conditions (Table 1, entries 5–11). In addition, the hydrogenation and decomposition of H_2O_2 were carried out. As shown in Fig. S11,† the H_2O_2 hydrogenation and decomposition rates on the Pd(111) surfaces were lower than those on the Pd(100) surfaces, indicating that H_2O_2 hydrogenation and decomposition were inhibited on the Pd(111) surfaces, in line with the observed higher H_2O_2 selectivity on $Pt_1Pd(111)/TiO_2$.

Fig. 2a–c and S12† show the catalytic activity as a function of reaction time for $Pd(111)/TiO_2$, $Pd(100)/TiO_2$, $Pt_1Pd(111)/TiO_2$, and $Pt_1Pd(100)/TiO_2$. The H_2 conversion (Fig. 2a) increased linearly with reaction time for all four catalysts. For example, the H_2 conversion over $Pt_1Pd(111)/TiO_2$ increased from 30.7% to 81.4% as the reaction time was extended from 10 to 60 min, which was higher than that of $Pt_1Pd(100)/TiO_2$ (16.0% to 57.2%), $Pd(100)/TiO_2$ (12.5% to 23.0%), and $Pd(111)/TiO_2$ (13.7% to 38.2%). Fig. 2b reveals that $Pt_1Pd(111)/TiO_2$ provided the highest H_2O_2 selectivity (~80%) with almost no degradation after 60 min of reaction. Fig. 2c and S12† show that the amount of generated H_2O_2, H_2O_2 concentration and H_2O_2 yield increased with reaction time for all four catalysts. An H_2O_2 concentration of 1.10% and H_2O_2 yield of 66.9% were achieved after 60 min of reaction over $Pt_1Pd(111)/TiO_2$. The amount of generated H_2O_2 was 2575.0 μmol in 60 min, which was 3.6, 5.0, and 1.8 times that of $Pd(111)/TiO_2$ (710.0 μmol), $Pd(100)/TiO_2$ (510.0 μmol), and $Pt_1Pd(100)/TiO_2$ (1402.5 μmol), respectively. In another set of experiments, the effect of the H_2/O_2 ratio on the DSHP was examined. As shown in Fig. 2d–f and S13,† the catalytic performance of the four catalysts, including the H_2 conversion, amount of H_2O_2, and H_2O_2 concentration, gradually increased when the ratio of H_2/O_2 was increased from 1 : 10 to 1 : 2. However, the H_2O_2 selectivity gradually decreased as the H_2/O_2 ratio increased, and when the H_2/O_2 ratio was lower than 1 : 8, the H_2O_2 selectivity was capable of reaching 100%. Moreover, the optimal H_2O_2 yield could be obtained when the H_2/O_2 ratio was 1 : 3. The performance on the Pd(111) surface was always better than on the Pd(100) surface, and the performance of the catalysts with single Pt atoms was always greater than those without single Pt atoms. All the above results indicate that the DSHP catalytic activity displays a facet-dependence and that it is more favorable on Pd(111) than Pd(100).

In order to evaluate the influence of the Pt content on the reaction, catalysts with similar Pd content (~3.5 wt%) and different Pt contents (0.07 to 0.17 wt%) were prepared, and each sample was characterized accordingly using ICP-OES and XRD (Table S1 and Fig. S14†). The DSHP activity measurements across the range of Pt content showed a volcano-like trend (Fig. 2g–i and S15a†). The optimal catalytic performance was obtained at a Pt/Pd ratio of 1 : 80, while the H_2O_2 selectivity remained almost the same throughout (~80%), implying that the addition of single Pt atoms produced a large increase in the catalytic activity and selectivity. However, the results of H_2O_2 hydrogenation indicated that the hydrogenation rate increased (from 1.1 to 8.9 mol g_{Pd}^{-1} h^{-1}) as the Pt content increased (Fig. S15b†), while Fig. S15c† shows that the addition of Pt can suppress the decomposition of H_2O_2. Furthermore, the DSHP activity of the $Pt_1Pd(111)/TiO_2$ catalyst in four different solvents was investigated, including H_2O, CH_3OH, C_2H_5OH, and 30% H_2O + 70% CH_3OH. The results in Fig. S16† show that alcohols

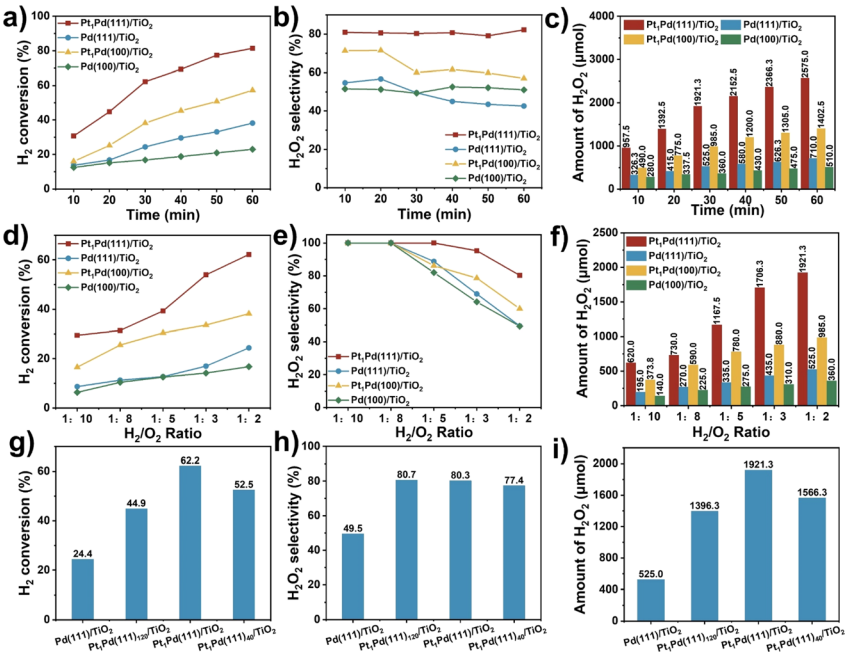

Fig. 2 Comparison of (a) H_2 conversion, (b) H_2O_2 selectivity and (c) amount of H_2O_2 as a function of H_2O_2 synthesis reaction time. Comparison of (d) H_2 conversion, (e) H_2O_2 selectivity and (f) amount of H_2O_2 at different H_2/O_2 ratios. Comparison of (g) H_2 conversion, (h) H_2O_2 selectivity and (i) amount of H_2O_2 at different Pd/Pt atomic ratios. Reaction conditions: 10 mL CH_3OH, 0.02 M HCl, 2.9 MPa 5% H_2/N_2, 1.1 MPa 25% O_2/N_2, T = 0 °C, catalyst weight: 10 mg, stirring: 1200 rpm, reaction time: 30 min.

are beneficial for improving the DSHP catalytic activity, with methanol being the best solvent and H_2O resulting in the lowest activity due to the fact that short-chain alcohols facilitate the mass transfer of H_2.[40] Eventually, the stability of $Pt_1Pd(111)/TiO_2$ was tested whilst the H_2 conversion was maintained at ~30%. As show in Fig. S17,† the catalytic activity remained almost unchanged after five cycles of testing, and the amount of generated H_2O_2 remained at ~1000 μmol, showing extraordinary stability. The morphology (Fig. S18†) and metal content (Table S1†) of $Pt_1Pd(111)/TiO_2$ remained almost unchanged after the reaction.

Finally, utilizing the H_2O_2 solution in the Fenton system, pollutants (*e.g.*, rhodamine B) can be effectively removed. Rhodamine B was added to the H_2O_2 solution together with $FeCl_2$. Afterwards, the rhodamine B was totally degraded, as evidenced by color changes and UV-visible spectroscopy (Fig. S19 and S20†).

Spectroscopy of catalysts

To understand the enhancement mechanism in detail, the CO binding strength of the catalysts with different exposed facets was investigated at ambient pressure using IR spectroscopy (Fig. 3). The signals in Fig. 3a–d were basically steady after purging for 30 minutes, and the peaks of CO absorption on the four catalysts at ~1978 and ~1886 cm^{-1} were ascribed to the bridged ($CO–Pd_2$) and threefold hollow ($CO–Pd_3$) configurations, respectively,[41,42] indicating that the Pd species mainly exist as metallic Pd. However, a weak peak at 2078 cm^{-1} across $Pt_1Pd(111)/TiO_2$ and $Pt_1Pd(100)/TiO_2$ was observed and can be assigned to linearly absorbed CO on the Pt atoms.[43,44] This peak was not observed on $Pd(111)/TiO_2$ and $Pd(100)/TiO_2$ (Fig. 3e–i), suggesting that the Pt species exist as single atoms on $Pt_1Pd(111)/TiO_2$ and $Pt_1Pd(100)/TiO_2$.

To probe the local electronic states and coordination structures of the Pt and Pd atoms in the different exposed facet catalysts, X-ray adsorption spectroscopy (XAS) was carefully performed. As shown in Fig. 4a, the Pd K-edge X-ray absorption near edge structure (XANES) of $Pt_1Pd(111)/TiO_2$ and $Pt_1Pd(100)/TiO_2$ was similar to that of Pd foil, indicating that the Pd species exist in a metallic state. In addition, the near-edge features of $Pt_1Pd(111)/TiO_2$ shifted to a lower valence state compared to that of $Pt_1Pd(100)/TiO_2$, indicating the existence of slightly electron-rich Pd species, which is beneficial for H_2O_2 synthesis.[45] Fig. 4b shows the Fourier-transform extended X-ray absorption fine structure (EXAFS) spectra of Pd foil, $Pt_1Pd(111)/TiO_2$, and $Pt_1Pd(100)/TiO_2$, with the main peak at 2–3 Å arising from Pd–Pd/Pt bonding (yellow region in Fig. 4b).[46] The results were further confirmed by the *K*-space spectra (Fig. S21†) and wavelet transform (WT) for the Pd K-edge (Fig. 4c). The Pt L3-edge XANES and EXAFS spectra were consistent with that of Pd. The Pt L3-edge XANES in Fig. 4d shows that the valence state of the Pt species in $Pt_1Pd(111)/TiO_2$ is higher than that in $Pt_1Pd(100)/TiO_2$. The EXAFS of $Pt_1Pd(111)/TiO_2$ and $Pt_1Pd(100)/TiO_2$ in Fig. 4e have two peaks at 2.2 and 3.1 Å, which were assigned to Pt–Pd bonding and Pt–Pd–Pt bonding, respectively,[47] which was further confirmed by the *K*-space spectra (Fig. S22†) and wavelet transform (WT) (Fig. 4f). The fitting parameters (Fig. S23, S24 and Tables S2, S3†), including the coordination number and bond length, suggested a stronger interaction exists between the Pd and Pt species on Pd(111) than on Pd(100), indicating a greater amount of electron transfer occurs in $Pt_1Pd(111)/TiO_2$.

X-ray photoelectron spectroscopy (XPS) was carried out on Pd 3d, as shown in Fig. S25.† The peaks at 340.5 and 335.3 eV of $Pd(111)/TiO_2$ assigned to the Pd $3d_{3/2}$ and Pd $3d_{5/2}$ orbitals shift to a lower binding energy than is observed in $Pd(100)/TiO_2$ (340.6 and 335.4 eV, respectively). Similarly, after adding the single Pt atoms, the peaks Pd $3d_{3/2}$ and Pd $3d_{5/2}$ of $Pt_1Pd(111)/$

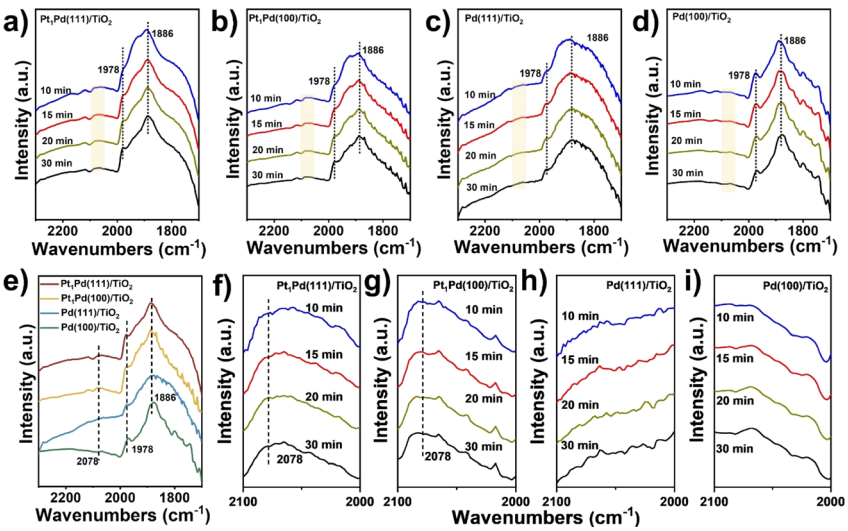

Fig. 3 DRIFT spectra of CO adsorption on (a) $Pt_1Pd(111)/TiO_2$, (b) $Pt_1Pd(100)/TiO_2$, (c) $Pd(111)/TiO_2$ and (d) $Pd(100)/TiO_2$ at room temperature at different time points. (e) Comparison of CO-DRIFT spectra at 30 min. (f–i) Magnified CO-DRIFT spectra between 2000 and 2100 cm^{-1} from (a), (b), (c) and (d), respectively.

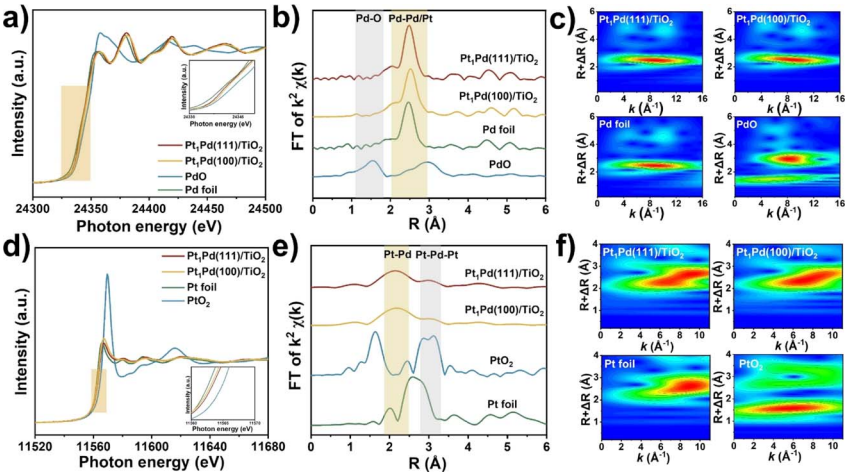

Fig. 4 (a) Pd K-edge XANES profiles in R space. (b) Pd extended X-ray absorption fine structure (EXAFS) spectra. (c) Wavelet transform (WT) for the Pd K-edge of $Pt_1Pd(111)/TiO_2$, $Pt_1Pd(100)/TiO_2$, Pd foil, and PdO. (d) Pt L3-edge XANES profiles in *R* space. (e) Pt extended X-ray absorption fine structure (EXAFS) spectra. (f) Wavelet transform (WT) for the Pt L3-edge of $Pt_1Pd(111)/TiO_2$, $Pt_1Pd(100)/TiO_2$, Pt foil, and PtO_2.

TiO_2 (340.3 and 335.1 eV, respectively) still appear at lower energy than those of $Pt_1Pd(100)/TiO_2$ (340.5 and 335.3 eV, respectively). In summary, the aforementioned results indicated that the Pd(111) and Pd(100) surfaces featured different electronic environments, with more electrons enriched on the Pd(111) surfaces, which is more favorable for dissociation of H_2, as discussed below.[48] Moreover, the addition of single Pt atoms enabled the peaks of the Pd species to shift to lower binding energies, favoring H_2O_2 synthesis.

Kinetics and isotope experiments

Herein, the effects of stirring rate, catalyst weight, reaction time, temperature, and H_2 pressure on the DSHP in the critical kinetic region were systematically evaluated. Control experiments were performed by varying stirring rate and catalyst weight to exclude the impacts of external diffusion. Fig. S26† shows that the H_2O_2 concentration was basically unchanged (~0.8 wt%) when the stirring rate was higher than 1200 rpm (1200 rpm was selected in our experiments). Furthermore, Fig. S27† shows that the H_2 conversion is linearly correlated to the catalyst weight. Thus, the above results imply that the DSHP reaction was kinetically controlled and was not dependent on external diffusion.

As shown in Fig. 5a, the curve of $\ln(c(H_2)\ \text{mol L}^{-1})$ as a function of reaction time (min) gave a straight line, indicating a pseudo first-order reaction with respect to the DSHP. The $Pt_1Pd(111)/TiO_2$ (0.027 min^{-1}) and $Pd(111)/TiO_2$ (0.007 min^{-1}) catalysts showed higher apparent rate constants than $Pt_1Pd(100)/TiO_2$ (0.014 min^{-1}) and $Pd(100)/TiO_2$ (0.003 min^{-1}), indicating that the catalysts with Pd(111) facets exhibited higher activity than those with Pd(100) facets. The apparent rate constant for the DSHP using D_2 was obtained for $Pt_1Pd(111)/TiO_2$, as shown in Fig. S28.† An obvious kinetic isotope effect (KIE) of k_{H_2}/k_{D_2} at 3.0 was identified, suggesting that H_2 activation contributes to the rate-determining step. The Arrhenius plots in Fig. 5b show that the apparent activation energy values (E_a) for $Pt_1Pd(111)/TiO_2$ (11.1 kJ mol^{-1}) and $Pd(111)/TiO_2$ (21.4 kJ mol^{-1}) were lower than those for $Pt_1Pd(100)/TiO_2$ (14.0 kJ mol^{-1}) and $Pd(100)/TiO_2$ (22.1 kJ mol^{-1}). Notably, a preferential H_2O_2 synthesis activity (H_2 reaction order of 1.7 for $Pt_1Pd(111)/TiO_2$ and 2.1 for $Pd(111)/TiO_2$, Fig. 5c) was achieved over the catalysts with the Pd(111) facets, which was lower than those achieved over the catalysts with Pd(100) facets (H_2 reaction order of 1.8 for $Pt_1Pd(100)/TiO_2$ and 2.2 for Pd(100)/

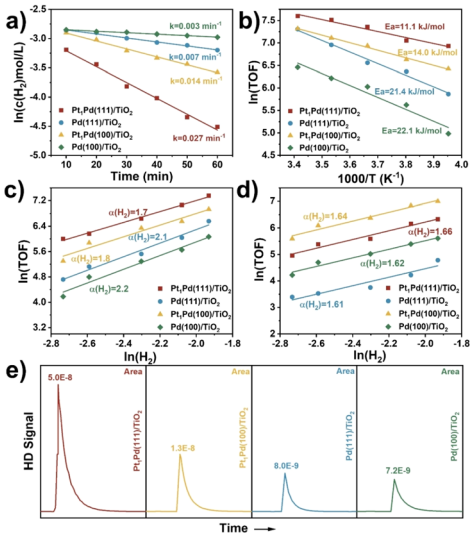

Fig. 5 (a) The apparent rate constant and (b) the experimental Arrhenius plots for H_2O_2 synthesis. H_2 reaction orders of (c) H_2O_2 synthesis and (d) H_2O_2 hydrogenation. (e) HD signal in H_2-D_2 exchange experiments at room temperature. 5% H_2/N_2 (20 mL min^{-1}) as carrier and D_2 (10 mL min^{-1}) as pulse gas, 100 μL quantitative ring, catalysts: 50 mg. The apparent rate constant (*k*) is the slope of the corresponding fitted curve. The TOF was the number for moles of H_2 converted on one mole of Pd per unit time. The H_2 reaction orders (α) is the slope of the corresponding fitted curve. The E_a is the slope of the corresponding fitted curve multiplied by −8.314.

TiO_2). This implies that the DSHP on the catalysts with Pd(111) facets were more favorable than on those with Pd(100) facets. Fig. 5d illustrates that the four catalysts share a similar H_2 reaction order (~1.6), meaning that the hydrogenation of H_2O_2 is not a dominant step affecting the H_2O_2 selectivity. H_2–D_2 exchange experiments were also conducted to investigate the ability of H_2 activation on $Pt_1Pd(111)/TiO_2$, $Pt_1Pd(100)/TiO_2$, $Pd(111)/TiO_2$, and $Pd(100)/TiO_2$. As shown in Fig. 5e, the HD peaks of $Pt_1Pd(111)/TiO_2$ and $Pd(111)/TiO_2$ were much higher than those of $Pt_1Pd(100)/TiO_2$ and $Pd(100)/TiO_2$, indicating that H_2 activation on the Pd(111) surface was more favorable than on the Pd(100) surface, leading to a higher H_2 conversion rate on catalysts with Pd(111) facets. Furthermore, the above kinetics and isotope experiments also indicated that the catalysts with single Pt atoms were favorable for H_2O_2 synthesis.

Density-functional theory calculations

Based on the above reactivity and characterization results, we have developed $Pt_1Pd(111)/TiO_2$ catalysts with superior catalytic activity relating to the exposed facets. To better understand the how the different exposed facets, Pd(111) and Pd(100), affect the reaction mechanism density-functional theory (DFT) calculations were performed. The simulation models (Fig. S29†) of $Pt_1Pd(111)/TiO_2$ and $Pt_1Pd(100)/TiO_2$ were built according to the reflections obtained from the AC HAADF STEM and EXAFS analyses. To determine the H_2 adsorption site, the adsorption energies of H_2 at different Pd sites over $Pt_1Pd(111)/TiO_2$ were calculated (the corresponding adsorption models are shown in Fig. S30a–c).† Fig. S31a† shows that the adsorption energies of H_2 at Pd^0 (the Pd site connected to the Pt atom), Pd1 (the Pd site away from the Pt atom), and Pd^{1+} (the Pd site further away from the Pt atom) were −0.45, −0.31, and −0.20 eV, respectively, indicating that H_2 was preferentially adsorbed on the Pd sites connected to the Pt atom. Moreover, H_2 was also preferentially adsorbed on the Pd^0 site over O_2 (adsorption energies of −0.30 eV), as shown in Fig. S30d and S31b.† Thus the possible elementary steps and mechanism of the DSHP on $Pt_1Pd(111)/TiO_2$ are proposed in Fig. 6a. Firstly, H_2 is adsorbed on the $Pt_1Pd(111)/TiO_2$ surface ($* + H_2 \rightarrow *H_2$) followed by dissociation into 2*H absorbed on a Pd site ($*H_2 \rightarrow *H + *H$). Then O_2 is

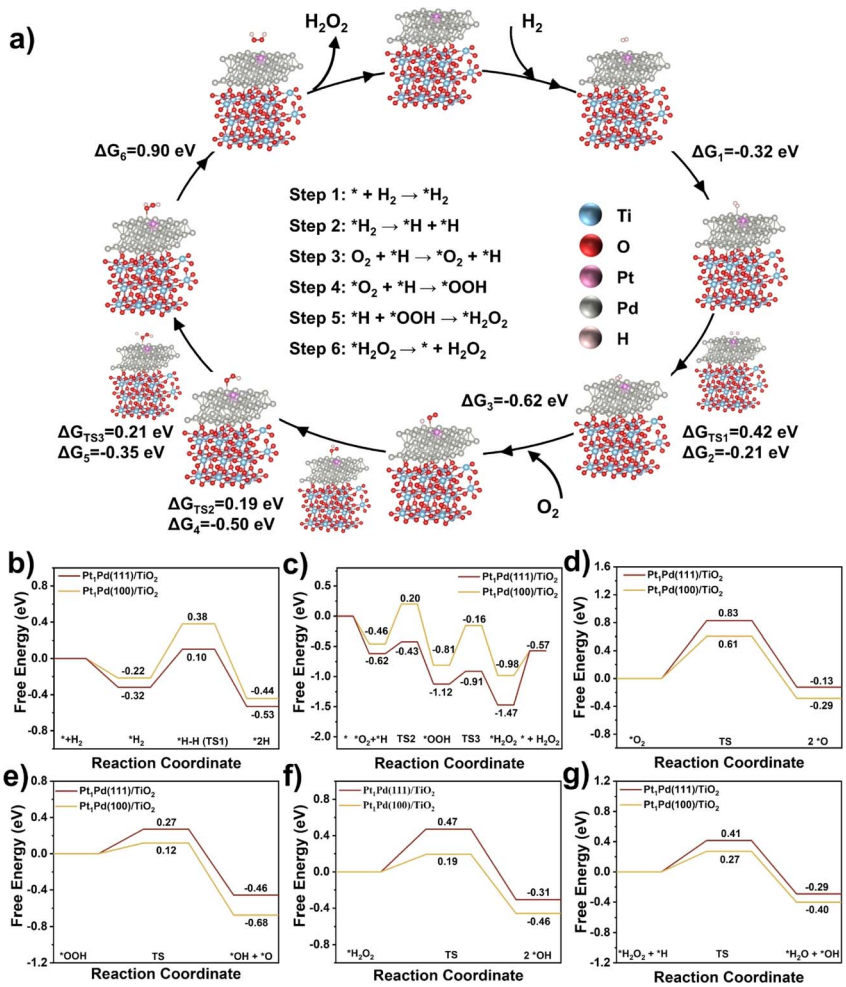

Fig. 6 DFT calculations and proposed mechanism. (a) The possible elementary steps and catalytic mechanism over $Pt_1Pd(111)/TiO_2$ for the DSHP. (b) Free energy profiles for (a) H_2 dissociation, (c) O_2 hydrogenation, (d) $*O_2$ dissociation, (e) *OOH dissociation, (f) $*H_2O_2$ dissociation, and $*H_2O_2$ hydrogenation on the $Pt_1Pd(111)/TiO_2$ and $Pt_1Pd(100)/TiO_2$ surfaces. TS: transition state.

adsorbed on the $Pt_1Pd(111)/TiO_2$ surface (O_2 + *H → *O_2 + *H) reacting with the adjacent *H to form *OOH (*O_2 + *H → *OOH). Subsequently, *OOH combines with another *H to form * H_2O_2 (*OOH + *H → *H_2O_2), and finally H_2O_2 is desorbed from the $Pt_1Pd(111)/TiO_2$ surface (*H_2O_2 → * + H_2O_2).

The corresponding free energies on the surface of $Pt_1Pd(111)/TiO_2$ and $Pt_1Pd(100)/TiO_2$ were investigated. The results from Fig. 6a, b, and S32† show that H_2 was more readily adsorbed on the $Pt_1Pd(111)/TiO_2$ (−0.32 eV) surface than on the $Pt_1Pd(100)/TiO_2$ (−0.22 eV). On the $Pt_1Pd(111)/TiO_2$ surface, the cleavage of the H–H bond has to overcome an energy barrier of 0.42 eV, which is lower than that on $Pt_1Pd(100)/TiO_2$ (0.60 eV). Therefore, H_2 dissociated more readily on $Pt_1Pd(111)/TiO_2$, providing a hydrogen source for the subsequent O_2 hydrogenation. The two-step O_2 hydrogenation to produce H_2O_2 is described in Fig. 6a, c, and S33.† The energy barriers for the first (*O_2 + *H → *OOH) and second (*OOH + *H → *H_2O_2) hydrogenation of O_2 on $Pt_1Pd(100)/TiO_2$ were found to be 0.66 and 0.65 eV, respectively. In contrast, the energy barriers of 0.19, 0.21 eV, respectively, on $Pt_1Pd(111)/TiO_2$ were lower. The corresponding reaction energies were also lower than on $Pt_1Pd(100)/TiO_2$ (−0.50 *vs.* −0.35 eV and −0.35 *vs.* −0.17 eV, respectively). However, the free energy of H_2O_2 desorption on the $Pt_1Pd(111)/TiO_2$ (0.90 eV) surface was higher than that of the $Pt_1Pd(100)/TiO_2$ (0.41 eV) surface. The above investigations of the transition states demonstrated that the whole DSHP process had a lower energy barrier on $Pt_1Pd(111)/TiO_2$ with H_2 dissociation assumed to be the rate determining step, in agreement with the experimental observations. Based on the DFT calculations, it could be concluded that $Pt_1Pd(111)/TiO_2$ presents an elevated ability to cleave the H–H bond in H_2 and O_2 hydrogenation, which strongly promoted the formation of H_2O_2, leading to enhanced DSHP performance with an obvious facet dependence.

Next, we simulated the four main side reactions, including *O_2 dissociation (*O_2 → 2 *O), *OOH dissociation (*OOH → *OH + *O), *H_2O_2 dissociation (*H_2O_2 → 2 *OH), and *H_2O_2 hydrogenation (*H_2O_2 + *H → *H_2O + *OH). The corresponding free energies, energy barriers, and structures are depicted in Fig. 6d–g and S34–37.† On $Pt_1Pd(111)/TiO_2$, the energy barriers of the four side reactions were 0.83, 0.27, 0.47, and 0.41 eV, respectively, which were greater than those of the corresponding competitive reactions (two-step O_2 hydrogenation to H_2O_2), indicating high H_2O_2 selectivity on $Pt_1Pd(111)/TiO_2$. In addition, $Pt_1Pd(100)/TiO_2$ showed lower energy barriers than $Pt_1Pd(111)/TiO_2$ for the four side reactions (0.61, 0.12, 0.19, and 0.27 eV), which implies that the H_2O_2 selectivity on $Pt_1Pd(111)/TiO_2$ could be higher than that on $Pt_1Pd(100)/TiO_2$, in agreement with the experimental results showing an obvious facet dependence.

Conclusions

The selective production of H_2O_2 in high amounts is a challenge in the DSHP. In this contribution, we propose a single Pt atom-modified Pd nanocrystal catalyst to efficiently synthesize H_2O_2. The as-prepared $Pt_1Pd(111)/TiO_2$ catalyst presents outstanding reactivity, producing 1921.3 μmol of H_2O_2 (the highest amount of H_2O_2 compared to previous reports), a H_2 conversion of 62.2%, and a H_2O_2 selectivity of 80.3% during the DSHP for 30 min. These results are better than those obtained for $Pt_1Pd(100)/TiO_2$, showing that the reaction exhibits a prominent facet dependence. Kinetic and isotopic results confirm that the remarkable activity of $Pt_1Pd(111)/TiO_2$ is attributed to the electron-rich structure of the Pd(111) surface, which contributes to H_2 activation, the rate-determining step in the DSHP process. The introduction of single Pt atoms also contributes to the synthesis of H_2O_2. DFT calculations confirm that the energy barriers for H_2 dissociation and the two-step O_2 hydrogenation on the $Pt_1Pd(111)$ surface are lower than on the $Pt_1Pd(100)$ surface. Furthermore, the energy barriers of the four side reactions (*O_2 dissociation, *OOH dissociation, *H_2O_2 dissociation, and *H_2O_2 hydrogenation) on the $Pt_1Pd(111)$ surface are larger than on $Pt_1Pd(100)$, resulting in higher selectivity and the production of greater amounts of H_2O_2 on $Pt_1Pd(111)/TiO_2$. This work provides a promising strategy to design and develop highly active DSHP catalysts, and deepens our understanding of the reaction mechanism.

Materials and methods

Chemicals

Potassium tetrachloropalladate (K_2PdCl_4), chloroplatinic acid ($H_2PtCl_6 \cdot 6H_2O$), and methanol (HPLC grade) were purchased from Energy Chemical. Hydrogen peroxide (30%) and acetone were purchased from Guangzhou Chemical Reagent Factory. L-Ascorbic acid, citric acid, potassium bromide (KBr), and polyvinyl pyrrolidone (PVP) were purchased from Shanghai Aladdin Biochemical Technology Co., Ltd. Titanium oxide (TiO_2, P25) and ferroin indicator were purchased from Shanghai Macklin Biochemical Co. Ltd. Cerous sulfate ($Ce(SO_4)_2$, 0.1 mol L^{-1}) was purchased from Tan–Mo Technology Co. Ltd.

Catalyst preparation

Synthesis of the $Pt_1Pd(111)$ nanocrystals: the $Pt_1Pd(111)$ nanocrystals were synthesized according to a slightly modified previous report.[37] 105 mg of PVP, 60 mg of citric acid, and 60 mg of L-ascorbic acid were added into a 3-neck flask containing 8 mL of deionized water at room temperature. Then the 3-neck flask equipped with a reflux condenser was heated to 120 °C and stirred for 5 min in an oil bath. Meanwhile, 65 mg of K_2PdCl_4 and 10 μL of $H_2PtCl_6 \cdot 6H_2O$ solution (0.1 g mL^{-1}) were dissolved in 3 mL of deionized water. The mixed solution was injected into the 3-necked flask *via* a peristaltic pump at 5 mL h^{-1}. Finally, the reaction was continued and stirred in air for 3 h at 120 °C. After the reaction, the samples were washed with acetone/deionized water three times to remove the excess molecules by centrifugation. Thus the $Pt_1Pd(111)$ nanocrystals were obtained.

Synthesis of $Pt_1Pd(111)/TiO_2$: the pre-prepared $Pt_1Pd(111)$ nanocrystals were suspended in 5 mL of deionized water and then dropped into 10 mL of deionized water containing 0.5 g of TiO_2 under vigorous stirring at room temperature. After stirring

for 4 h, the temperature was increased to 80 °C in order to evaporate the deionized water. Finally, the samples were obtained after calcining.

Synthesis of $Pt_1Pd(100)$ nanocrystals: 105 mg of PVP, 300 mg of KBr, and 60 mg of L-ascorbic acid were added into a 3-neck flask containing 8 mL of deionized water at room temperature. Then the 3-neck flask equipped with a reflux condenser was heated to 80 °C and stirred for 5 min in an oil bath. Meanwhile, 65 mg of K_2PdCl_4 and 10 μL of $H_2PtCl_6 \cdot 6H_2O$ solution (0.1 g mL^{-1}) were dissolved in 3 mL of deionized water. The mixed solution was then added into the 3-necked flask and stirred for 3 h at 80 °C. After the reaction, the samples were washed with acetone/deionized water three times to remove the excess molecules by centrifugation. Thus the $Pt_1Pd(100)$ nanocrystals were obtained.

Synthesis of $Pt_1Pd(100)/TiO_2$: the preparation process was similar to that of $Pt_1Pd(111)/TiO_2$. $Pd(111)/TiO_2$, $Pt_1Pd(111)_{40}/TiO_2$, and $Pt_1Pd(111)_{120}/TiO_2$ were synthesized by the same method as $Pt_1Pd(111)/TiO_2$. $Pd(100)/TiO_2$ was synthesized by the same method as $Pt_1Pd(100)/TiO_2$.

Catalyst characterization

Inductively coupled plasma optical emission spectrometry was used to determine the metal loadings of all catalysts (ICP-OES, Agilent 7700). X-ray photoelectron spectroscopy (Thermo Fisher Nexsa) was used to evaluate the valence states of the catalysts, and the data was processed using the XPSPEAK software. The X-ray diffraction patterns were produced on a LIFM-X-ray powder diffractometer (Smart Lab) using s Cu Kα (λ = 0.15432 nm) beam, and the data was processed and compared with PDF cards using the MDI Jade 6 software. Transmission electron microscopy (TEM) and scanning transmission electron microscopy (STEM) images were captured on a FEI Tecnai G2 F30 transmission electron microscope using an acceleration voltage of 300 kV. The high-resolution TEM, aberration-corrected high-angle annular darkfield STEM, and energy dispersive X-ray (EDX) spectrometry mapping were produced using a JEM-ARM200F transmission electron microscope equipped with double spherical aberration correctors. Pd K-edge and Pt L_3-edge extended X-ray absorption fine structure spectrometry (EXAFS) were performed at the BL14W1 beamline of the Shanghai Synchrotron Radiation Facility. The incident beam was monochromatized using a Si (311) double-crystal monochromator while the high harmonics of the monochromatic beam were diminished. EXAFS data analysis was carried out on the Demeter software employing the conventional processes: background removal, normalization and Fourier transformation of the EXAFS oscillations. A Shimadzu UV2600 spectrophotometer with wavelength precision of 0.3 nm was used to collect the UV-Vis spectra. The *in situ* diffuse reflectance infrared Fourier-transform spectra (DRIFTS) of CO absorption were measured on a Nicolet iS50 (Thermo Science) with an *in situ* transmission cell. The catalysts were reduced at 200 °C in a 20% H_2/N_2 atmosphere for 1 hour before the test. The background was collected under N_2 after reduction. At this point, 10% CO/N_2 was introduced for 30 minutes, and the adsorption spectrum was recorded until there was no change in the spectrum. Finally, N_2 was employed to sweep away the physically adsorbed CO species, while the spectrum was obtained. H_2-D_2 exchange experiments were performed on a continuous flow fixed bed at room temperature and atmospheric pressure. The catalysts were loaded in a quartz tube with an inner diameter of 7 mm. Pure D_2 with a flow rate of 10 mL min^{-1} was used as the pulse gas with a 100 μL quantitative ring, and 5% H_2/N_2 with a flow rate of 20 mL min^{-1} was used as the carrier gas. HD signals ($m/z = 3$) were recorded online using mass spectrometry (Hiden Analytical HPR-20 QIC benchtop Gas Analysis System). The H_2 reaction orders were calculated using the turnover frequency (TOF) values obtained at different H_2 partial pressures. The Arrhenius plots were calculated using the turnover frequency (TOF) values obtained at different temperatures (−20, −10, 0, 10, and 20 °C). The apparent rate constants were calculated using the H_2 concentration after reaction at the corresponding reaction time (10, 20, 30, 40, 50, and 60 min).

Catalytic performance test

The direct synthesis of H_2O_2 was carried out in a stainless-steel autoclave with a nominal volume of 100 mL and a digital pressure gauge. A solution, containing 10 mL of methanol, 0.02 M HCl, and 10 mg of catalyst, was encapsulated in the autoclave to assess the catalytic performance of the catalysts for H_2O_2 synthesis. The autoclave was sealed and then charged with 1.1 MPa 25% O_2/N_2 (7.30 mmol O_2) and 2.9 MPa 5% H_2/N_2 (3.85 mmol H_2) at room temperature, following purging with 0.7 MPa 5% H_2/N_2three times. After cooling to 0 °C in an ice-water bath, the reaction mixture was stirred at 1200 rpm for 30 minutes. The hydrogen content before and after the reaction was calculated using a gaseous chromatograph (GC) equipped with a thermal conductivity detector (TCD) and a TDX-01 column. The amount of H_2O_2 was determined by titrating aliquots of the final solution with acidified cerium sulfate standard solution ($Ce(SO_4)_2$, 0.01 mol L^{-1}) in the presence of three drops of ferroin indicator solution. The H_2 conversion, H_2O_2 selectivity, and H_2O_2 productivity were calculated as follows:

$$H_2 \text{ conversion } (\%) = \frac{n(H_2)_{in} - n(H_2)_{out}}{n(H_2)_{in}} \times 100 \quad (1)$$

$$H_2O_2 \text{ selectivity } (\%) = \frac{n(H_2O_2)_{detected}}{n(H_2)_{in}} \times 100\% \quad (2)$$

$$H_2O_2 \text{ productivity rate } \left(\text{mol } g_{Pd}^{-1}\ h^{-1}\right) = \frac{n(H_2O_2)_{detected}}{m_{Pd} \times \text{Time}} \times 100\%. \quad (3)$$

The hydrogenation of H_2O_2 was performed in a stainless-steel autoclave using the same procedure as for the synthesis of H_2O_2. 10 mL of methanol, 250 μL of H_2O_2 (~30 wt%, 2.56 mmol), 0.02 M HCl, and 10 mg of catalyst were encapsulated in the autoclave. The sealed autoclave was then charged with 2.9 MPa 5% H_2/N_2 after purging with 0.7 MPa 5% H_2/N_2 three

times at room temperature. The reaction mixture was stirred for 30 minutes at 1200 rpm after being cooled in an ice-water bath to 0 °C. The hydrogenation of H_2O_2 was determined by titrating aliquots of the final solution with acidified cerium sulfate standard solution ($Ce(SO_4)_2$, 0.002 mol L^{-1}) in the presence of three drops of ferroin indicator solution after the reaction. The H_2O_2 hydrogenation rate was calculated as follows:

$$H_2O_2 \text{ hydrogenation } \left(\text{mol } g_{Pd}^{-1}\ h^{-1}\right) = \frac{n(H_2O_2)_{before} - n(H_2O_2)_{after}}{m_{Pd} \times \text{Time}} \times 100\%. \quad (4)$$

The decomposition of H_2O_2 was evaluated using a similar method as used for the hydrogenation of H_2O_2, except that 2.9 MPa 5% H_2/N_2 was replaced with 4 MPa N_2. The H_2O_2 decomposition rate was calculated as follows:

$$H_2O_2 \text{ decomposition } \left(\text{mol } g_{Pd}^{-1}\ h^{-1}\right) = \frac{n(H_2O_2)_{before} - n(H_2O_2)_{after}}{m_{Pd} \times \text{Time}} \times 100\%. \quad (5)$$

Computational methods

The Vienna *Ab Initio* Package (VASP)[49] was employed to perform all the density-functional theory (DFT) calculations within the generalized gradient approximation (GGA) using the PBE[50] formulation. The projected augmented wave (PAW) potentials were chosen to describe the ionic cores and take the valence electrons into account using a plane wave basis set with a kinetic energy cutoff of 520 eV. Partial occupancies of the Kohn–Sham orbitals were allowed using the Gaussian smearing method and a width of 0.05 eV. The electronic energy was considered self-consistent when the energy change was smaller than 10^{-5} eV. A geometry optimization was considered convergent when the force change was smaller than 0.03 eV $Å^{-1}$ and the spin polarization effect was included in the whole calculation. Grimme's DFT-D3 methodology was used to describe the dispersion interactions. The vacuum spacing perpendicular to the plane of the structure is 18 Å. The Brillouin zone integral uses the surface structures of 2 × 2 × 1 Monkhorst pack *K*-point sampling. Finally, the adsorption energies (E_{ads}) are calculated as $E_{ads} = E_{ad/sub} - E_{ad} - E_{sub}$, where $E_{ad/sub}$, E_{ad} and E_{sub} are the optimized adsorbate/substrate system, the adsorbate in the structure and the clean substrate respectively. The free energy is calculated as follows:

$$G = E + \text{ZPE} - \text{TS}, \quad (6)$$

where G, E, ZPE and TS are the free energy, total energy from the DFT calculations, zero-point energy and entropic contributions, respectively. The vibrational frequency was obtained by fixing the surface and releasing the adsorbed molecules. The zero-point energy was calculated as $\text{ZPE} = \sum_{i=1}^{3N} \frac{\hbar\omega_i}{2}$, where $\hbar$ is Planck's constant and ω_i is the frequency of the ith vibrational mode of the adsorbed molecule. The $TiO_2(101)$ and Pd(111), Pd(100) surfaces were used in our calculations.

Data availability

Additional details regarding experimental and calculation data are given in the ESI.†

Author contributions

The manuscript was written through the contributions of all authors. Xiaohui He and Ying Zhang developed the concept. Ying Zhang designed these experiments and analyzed experimental data. Ziyue Wang and Guanghui Guo contributed to the catalyst synthesis. Qingdi Sun contributed to the theoretical calculations. Hao Liu performed the EXAFS measurements and analyzed the data. Ying Zhang and Xiaohui He wrote the paper. Xiaohui He and Hongbing Ji directed the project. All the authors discussed the results and commented on the paper. All authors have approved the final version of the manuscript.

Conflicts of interest

There are no conflicts to declare.

Acknowledgements

This work was supported by the National Key Research and Development Program Nanotechnology Specific Project (No. 2020YFA0210900), Guangdong Natural Science Funds for Distinguished Young Scholar (2022B1515020035), the National Natural Science Foundation of China (22078371, U22A20428, 21961160741), the special fund for Science and Technology Innovation Teams of Shanxi Province (202304051001007), The authors thank the Shanghai Synchrotron Radiation Facility of China for the XAFS spectra measurements at the BL14W1 beamline, Guangdong Basic Research Center of Excellence for Functional Molecular Engineering, and the Chemistry and Chemical Engineering Guangdong Laboratory (Grant No. 1922010). Also, thanks go to eceshi (https://www.eceshi.com/s) for collecting the data of XPS and DRIFTS CO chemisorption.

References

1 K. Cao, H. Yang, S. Bai, Y. Xu, C. Yang, Y. Wu, M. Xie, T. Cheng, Q. Shao and X. Huang, *ACS Catal.*, 2021, **11**, 1106–1118.
2 L. Wang, J. Zhang, Y. Zhang, H. Yu, Y. Qu and J. Yu, *Small*, 2022, **18**, e2104561.
3 R. Svensson and H. Gronbeck, *J. Am. Chem. Soc.*, 2023, **145**, 11579–11588.
4 A. Huang, R. S. Delima, Y. Kim, E. W. Lees, F. G. L. Parlane, D. J. Dvorak, M. B. Rooney, R. P. Jansonius, A. G. Fink, Z. Zhang and C. P. Berlinguette, *J. Am. Chem. Soc.*, 2022, **144**, 14548–14554.
5 G. H. Han, S. H. Lee, S. Y. Hwang and K. Y. Lee, *Adv. Energy Mater.*, 2021, **11**, 2003121.

6 Z. Yang, Z. Wei, S. Zhou, B. Bao, S. Zhao and F. Gong, *Chem. Eng. J.*, 2023, **456**, 140915.
7 S. Yu, X. Cheng, Y. Wang, B. Xiao, Y. Xing, J. Ren, Y. Lu, H. Li, C. Zhuang and G. Chen, *Nat. Commun.*, 2022, **13**, 4737.
8 R. J. Lewis, M. Koy, M. Macino, M. Das, J. H. Carter, D. J. Morgan, T. E. Davies, J. B. Ernst, S. J. Freakley, F. Glorius and G. J. Hutchings, *J. Am. Chem. Soc.*, 2022, **144**, 15431–15436.
9 R. J. Lewis, K. Ueura, X. Liu, Y. Fukuta, T. Qin, T. E. Davies, D. J. Morgan, A. Stenner, J. Singleton, J. K. Edwards, S. J. Freakley, C. J. Kiely, L. Chen, Y. Yamamoto and G. J. Hutchings, *ACS Catal.*, 2023, **13**, 1934–1945.
10 G. V. Fortunato, E. Pizzutilo, I. Katsounaros, D. Gohl, R. J. Lewis, K. J. J. Mayrhofer, G. J. Hutchings, S. J. Freakley and M. Ledendecker, *Nat. Commun.*, 2022, **13**, 1973.
11 S. Yang, A. Verdaguer-Casadevall, L. Arnarson, L. Silvioli, V. Čolić, R. Frydendal, J. Rossmeisl, I. Chorkendorff and I. E. L. Stephens, *ACS Catal.*, 2018, **8**, 4064–4081.
12 J. K. Edwards, S. J. Freakley, R. J. Lewis, J. C. Pritchard and G. J. Hutchings, *Catal. Today*, 2015, **248**, 3–9.
13 S. Shaybanizadeh, R. Luque and A. Najafi Chermahini, *Green Chem.*, 2022, **24**, 5524–5534.
14 H. C. Li, Q. Wan, C. Du, J. Zhao, F. Li, Y. Zhang, Y. Zheng, M. Chen, K. H. L. Zhang, J. Huang, G. Fu, S. Lin, X. Huang and H. Xiong, *Nat. Commun.*, 2022, **13**, 6072.
15 T. Richards, J. H. Harrhy, R. J. Lewis, A. G. R. Howe, G. M. Suldecki, A. Folli, D. J. Morgan, T. E. Davies, E. J. Loveridge, D. A. Crole, J. K. Edwards, P. Gaskin, C. J. Kiely, Q. He, D. M. Murphy, J.-Y. Maillard, S. J. Freakley and G. J. Hutchings, *Nat. Catal.*, 2021, **4**, 575–585.
16 G. M. Lari, B. Puertolas, M. Shahrokhi, N. Lopez and J. Perez-Ramirez, *Angew. Chem., Int. Ed.*, 2017, **56**, 1775–1779.
17 S. J. Freakley, Q. He, J. H. Harrhy, L. Lu, D. A. Crole, D. J. Morgan, E. N. Ntainjua, J. K. Edwards, A. F. Carley, A. Y. Borisevich, C. J. Kiely and G. J. Hutchings, *Science*, 2016, **351**, 965–968.
18 Z. Yang, Z. Hao, S. Zhou, P. Xie, Z. Wei, S. Zhao and F. Gong, *ACS Appl. Mater. Interfaces*, 2023, **15**, 23058–23067.
19 S. Wang, G. Jiang, Z. Yang, L. Mu, T. Ji, X. Lu and J. Zhu, *ACS Sustain. Chem. Eng.*, 2022, **10**, 13750–13758.
20 R. J. Lewis, K. Ueura, X. Liu, Y. Fukuta, T. E. Davies, D. J. Morgan, L. Chen, J. Qi, J. Singleton, J. K. Edwards, S. J. Freakley, C. J. Kiely, Y. Yamamoto and G. J. Hutchings, *Science*, 2022, **376**, 615–620.
21 Z. Jin, Y. Liu, L. Wang, C. Wang, Z. Wu, Q. Zhu, L. Wang and F.-S. Xiao, *ACS Catal.*, 2021, **11**, 1946–1951.
22 T. Ricciardulli, S. Gorthy, J. S. Adams, C. Thompson, A. M. Karim, M. Neurock and D. W. Flaherty, *J. Am. Chem. Soc.*, 2021, **143**, 5445–5464.
23 V. R. Naina, S. Wang, D. I. Sharapa, M. Zimmermann, M. Hähsler, L. Niebl-Eibenstein, J. Wang, C. Wöll, Y. Wang, S. K. Singh, F. Studt and S. Behrens, *ACS Catal.*, 2021, **11**, 2288–2301.
24 A. Barnes, R. J. Lewis, D. J. Morgan, T. E. Davies and G. J. Hutchings, *Catal. Sci. Technol.*, 2022, **12**, 1986–1995.
25 Y. Wang, M. Zheng, Y. Li, C. Ye, J. Chen, J. Ye, Q. Zhang, J. Li, Z. Zhou, X. Z. Fu, J. Wang, S. G. Sun and D. Wang, *Angew. Chem., Int. Ed.*, 2022, **61**, e202115735.
26 M. Ma, G. Li, W. Yan, Z. Wu, Z. Zheng, X. Zhang, Q. Wang, G. Du, D. Liu, Z. Xie, Q. Kuang and L. Zheng, *Adv. Energy Mater.*, 2022, **12**, 2103336.
27 J. Li, L. Sun, Q. Wan, J. Lin, S. Lin and X. Wang, *J. Phys. Chem. Lett.*, 2021, **12**, 11415–11421.
28 D. W. Flaherty, *ACS Catal.*, 2018, **8**, 1520–1527.
29 H. Zhang, X. Qiu, Y. Chen, S. Wang, S. E. Skrabalak and Y. Tang, *Small*, 2020, **16**, e1906026.
30 T. H. Yang, Y. Shi, A. Janssen and Y. Xia, *Angew. Chem., Int. Ed.*, 2020, **59**, 15378–15401.
31 G. Wang, Z. Yang, Y. Du and Y. Yang, *Angew. Chem., Int. Ed.*, 2019, **58**, 15848–15854.
32 M. Zhao, Z. Chen, Z. Lyu, Z. D. Hood, M. Xie, M. Vara, M. Chi and Y. Xia, *J. Am. Chem. Soc.*, 2019, **141**, 7028–7036.
33 G. Liu, W. Zhou, Y. Ji, B. Chen, G. Fu, Q. Yun, S. Chen, Y. Lin, P. F. Yin, X. Cui, J. Liu, F. Meng, Q. Zhang, L. Song, L. Gu and H. Zhang, *J. Am. Chem. Soc.*, 2021, **143**, 11262–11270.
34 W. Zhang, Y. Shi, Y. Yang, J. Tan and Q. Gao, *Chin. J. Catal.*, 2022, **43**, 3116–3125.
35 G. Fang, W. Li, X. Shen, J. M. Perez-Aguilar, Y. Chong, X. Gao, Z. Chai, C. Chen, C. Ge and R. Zhou, *Nat. Commun.*, 2018, **9**, 129.
36 Q. Sun, X. Wang, H. Wang, H. Zhang, Q. He, Y. Zhang, Y. Cheng, X. Zhang, S. Shi, L. Tao, X. He and H. Ji, *J. Mater. Chem. A*, 2022, **10**, 10837–10843.
37 R. Long, K. Mao, X. Ye, W. Yan, Y. Huang, J. Wang, Y. Fu, X. Wang, X. Wu, Y. Xie and Y. Xiong, *J. Am. Chem. Soc.*, 2013, **135**, 3200–3207.
38 L. F. de L. e Freitas, B. Puértolas, J. Zhang, B. Wang, A. S. Hoffman, S. R. Bare, J. Pérez-Ramírez, J. W. Medlin and E. Nikolla, *ACS Catal.*, 2020, **10**, 5202–5207.
39 D. Ding, X. Xu, P. Tian, X. Liu, J. Xu and Y.-F. Han, *Chin. J. Catal.*, 2018, **39**, 673–681.
40 A. Akram, G. Shaw, R. J. Lewis, M. Piccinini, D. J. Morgan, T. E. Davies, S. J. Freakley, J. K. Edwards, J. A. Moulijn and G. J. Hutchings, *Catal. Sci. Technol.*, 2020, **10**, 8203–8212.
41 D. Jiang, G. Wan, C. E. García-Vargas, L. Li, X. I. Pereira-Hernández, C. Wang and Y. Wang, *ACS Catal.*, 2020, **10**, 11356–11364.
42 L. Wang, S. Deo, A. Mukhopadhyay, N. A. Pantelis, M. J. Janik and R. M. Rioux, *ACS Catal.*, 2022, **12**, 12927–12941.
43 X. Li, X. I. Pereira-Hernandez, Y. Chen, J. Xu, J. Zhao, C. W. Pao, C. Y. Fang, J. Zeng, Y. Wang, B. C. Gates and J. Liu, *Nature*, 2022, **611**, 284–288.
44 J. Liu, F. R. Lucci, M. Yang, S. Lee, M. D. Marcinkowski, A. J. Therrien, C. T. Williams, E. C. H. Sykes and M. Flytzani-Stephanopoulos, *J. Am. Chem. Soc.*, 2016, **138**, 6396–6399.
45 N. M. Wilson, P. Priyadarshini, S. Kunz and D. W. Flaherty, *J. Catal.*, 2018, **357**, 163–175.
46 K. Guo, X. Han, S. Wei, J. Bao, Y. Lin, Y. Li and D. Xu, *Nano Lett.*, 2023, **23**, 1085–1092.
47 L. Zhang, H. Liu, S. Liu, M. Norouzi Banis, Z. Song, J. Li, L. Yang, M. Markiewicz, Y. Zhao, R. Li, M. Zheng, S. Ye,

Z.-J. Zhao, G. A. Botton and X. Sun, *ACS Catal.*, 2019, **9**, 9350–9358.
48 Y. Zhang, Y. Cheng, X. Wang, Q. Sun, X. He and H. Ji, *ACS Catal.*, 2022, **12**, 15091–15096.
49 G. Kresse and J. Furthmuller, *Phys. Rev. B: Condens. Matter Mater. Phys.*, 1996, **54**, 11169–11186.
50 J. P. Perdew, K. Burke and M. Ernzerhof, *Phys. Rev. Lett.*, 1996, **77**, 3865–3868.